Thermally induced chemical and structural transformations in thin cobalt films

Matteo Jugovac,[*,†,‡] Iulia Cojocariu,[†,‡,¶] Francesca Genuzio,[‡] Carlo Alberto Brondin,[‡,§] Vitaliy Feyer,[†,‖] Claus Michael Schneider,[†,‖] Andrea Locatelli,[‡] and Tevfik Onur Menteş[*,‡]

†*Peter Grünberg Institute (PGI-6), Forschungszentrum Jülich GmbH, 52425 Jülich, Germany*

‡*Elettra Sincrotrone Trieste, S.S. 14 km 163.5 in AREA Science Park, Basovizza, 34149 Trieste, Italy*

¶*Dipartmento di Fisica, Università degli studi di Trieste, 34127 Trieste, Italy*

§*Dipartmento di Scienze Molecolari e Nanosistemi, Università Ca' Foscari di Venezia, 30172 Venice, Italy*

‖*Fakultät f. Physik and Center for Nanointegration Duisburg-Essen (CENIDE), Universität Duisburg-Essen, 47048 Duisburg, Germany*

E-mail: matteo.jugovac@elettra.eu; tevfik.mentes@elettra.eu

Abstract

The effect of annealing and cooling on the structural properties of thin cobalt films possessing either *hcp*(0001) or *fcc*(100) crystalline arrangement is studied on clean and carbon-reconstructed W(110), respectively. The films grown on clean W(110) crystal present a surface with hexagonal symmetry and undergo the well-known *hcp-fcc* structural transition upon annealing to temperatures higher than 700 K, while after cooling down to room temperature, the film is characterized by a laterally-heterogeneous morphology featuring different stacking configurations. On the carbide-covered W(110), Co grows, instead, in a *fcc*(100) arrangement with a high level of disorder, for which annealing leads to an improved crystalline order. Further annealing to above 900 K induces an irreversible transition from *fcc*(100) to *hcp*(0001) stacking via domain nucleation and growth on a micrometer scale. This recrystallization process is accompanied by a change in the film's chemical composition and magnetic structure. The excess carbon resulting from the recrystallization leads to the growth of micrometer-sized graphene islands on top of the *hcp* regions.

Keywords: cobalt, transformation, stacking, graphene, crystallinity.

Introduction

Among the materials utilized for magnetic devices, cobalt films have attracted particular interest owing to their widespread use in magnetic storage media and spintronics devices.[1–3] The structural and morphological stability of thin cobalt films against phase transitions and understanding the consequences of interface alloying and chemistry are crucial for achieving desired electronic and magnetic properties. For instance, controlling the *fcc vs. hcp* phase fraction was shown to lead to notable effects on the magnetic anisotropy of Co films.[4] Notably, the temperature-induced phase transition from hexagonal close-packed (*hcp*) to face-centered cubic (*fcc*) crystalline arrangement occurring at around 690 K in bulk Co may also affect the grain morphology and stacking sequence in thin films and layered structures,[5] with consequences in magnetic properties[6–9]

Beyond crystal structure and stacking faults, surface and interface are well-known to influence the physical properties of Co films. The effect of the substrate on the magnetic anisotropy of Co ultrathin films was shown in several studies, including substrate modification by hydrogen in Co/Pt(111)[10] and alloying at the interface in Co/Ir(111).[11] Furthermore, substantial changes in perpendicular magnetic anisotropy were induced by surface adsorbates, in particular by carbon species such as graphene,[11] CO,[12] surface carbides[13] and C_{60}.[14] Therefore, understanding temperature-driven stacking changes along with carbon bulk dissolution and surface segregation occurring in cobalt are thus essential for tailoring the desired properties of Co thin films,[15] ahead of their future usage in various applications and devices. In this regard, achieving high-temperature stability of the film morphology and crystal structure is mandatory for ensuring long-lasting functionality in high-temperature conditions. In addition, the stability of cobalt films holds significant importance in graphene synthesis through chemical vapor deposition protocols.[16,17] A thorough understanding of temperature effects may facilitate achieving improvements in the crystallographic quality of both Co and graphene. Indeed, the temperature influences the nucleation and growth kinetics of graphene, as well as carbon diffusion and surface mobility. These factors collectively impact the size, coverage, and azimuthal orientation of the graphene domains[18] Moreover, the synthesis temperature may affect the graphene interaction with the cobalt film, inducing carbon interfacial segregation and graphene decoupling from substrate.[19]

In this work, we report on the temperature-dependent structural behavior of thin cobalt films. By employing low-energy electron microscopy (LEEM), x-ray photoemission spectroscopy (XPS), and micro low-energy electron diffraction (μLEED), we investigate the structural and chemical transformations occurring in thin cobalt films in the temperature range from ambient conditions to 900 K. In particular, we unravel the role of dissolved atoms inside the Co matrix on the crystalline arrangement of the film. To achieve this, clean and carbon-reconstructed W(110) surfaces were utilized as templates for the formation of ordered Co films in *hcp*(0001) and *fcc*(100) arrangements, respectively. A spectromicroscopy approach allowed to monitor the evolution of the *hcp-fcc* phase transition with high lateral resolution and to relate the film crystalline structure to the chemical changes within the Co matrix. The results highlight the role of dissolved carbon and tungsten in determining the structural and magnetic properties of the Co film.

Results and discussion

Co/W(110): *hcp* vs *fcc* structure

In order to characterize structural transformations in thin cobalt films, cobalt was deposited at room temperature on a clean W(110) surface for a nominal coverage of 50 monolayers (ML) - 10 nm. As visible in Figure 1a, the resulting surface after a mild annealing of the as-grown film presents a single Bragg peak centered at around V_{st} = 22.3 V in the low-energy electron reflectivity curve (LEEM-IV) of the (00) beam in normal incidence, while the corresponding μLEED pattern shows six sharp diffraction spots, both consistent with an unreconstructed (1x1) *hcp* surface.[20] The sample was, therefore, annealed while following the changes in LEEM (V_{st} = 22 V) at the onset of the Bragg peak (Figure 1b-g).

The as-grown film at room temperature shows a very low LEEM intensity due to the reduced electron reflectivity induced by the disorder (Figure 1b). Upon annealing (with a heating rate of about 2 K/s), the LEEM intensity rises as the crystalline order of the Co film improves. At about 710 K, tiny islands appear in LEEM as dark dots. This structure coalesces until this new phase entirely covers the surface.

At 793 K, LEEM-IV and µ-LEED patterns were acquired from the surface uniformly covered by the high-temperature phase (Figure 1h). The LEEM-IV data reveals that the Bragg peak is split into two components, in line with the typical LEEM-IV curves from a range of *fcc* stacked surface.[20] Also, considering that the *hcp-fcc* transition in bulk cobalt also occurs at about 690 K,[21] we assign the high-temperature phase to *fcc*(111) cobalt. Indeed, the *fcc*(111) stacking is also confirmed by the three-fold symmetry of the LEED pattern acquired upon completion of the phase transition (Figure 1h).

Upon cooling down the sample, *hcp*-stacked regions appear and grow as expected for a reversible *hcp-fcc* transition. In comparison to the appearance of *fcc* regions during annealing, *hcp* regions nucleate at a much lower temperature during cooldown, indicating a significant thermal hysteresis in the *hcp-fcc* transition, in line with previous reports.[22,23] We observed that the *fcc-hcp* transformation starts at around 500 K and proceeds with the formation of small patches having several LEEM contrast levels, as seen in Figure 2. Even at room temperature, the LEEM contrast remains heterogeneous (Figure 3a).

In order to understand the nature of the heterogeneity observed at room temperature, three distinctly different areas are identified (as marked by A, B and C in Figure 3a) and LEEM-IV curves were acquired from each area (Figure 3b). All three regions are characterized by a prominent Bragg peak centered at about V_{st} = 23-24 V. Region A presents the characteristic reflectivity curve of an *hcp*-stacked surface with a simple featureless Bragg peak. However, the curves (describing regions B and C) exhibit a shoulder with varying intensity on the low-energy side of the Bragg peak. In earlier LEEM-IV studies on the homoepitaxial growth on Ag(111), changes in the shape of the Bragg peak were associated with stacking faults in a nominally *fcc*(111) film, with the intensity variations in the shoulder feature at lower energy, indicating the distance of the mis-stacked layer from the surface.[20] Monitoring similar changes this time for a nominally *hcp*(0001) film, we attribute the LEEM-IV curves from regions B and C to the presence of *fcc* stacked layers below or at the surface of the *hcp* film. This is consistent with stacking faults within the *hcp* film, which were reported to be kinetically frozen remnants of the *fcc* phase.[24] Nevertheless, given the limited inelastic

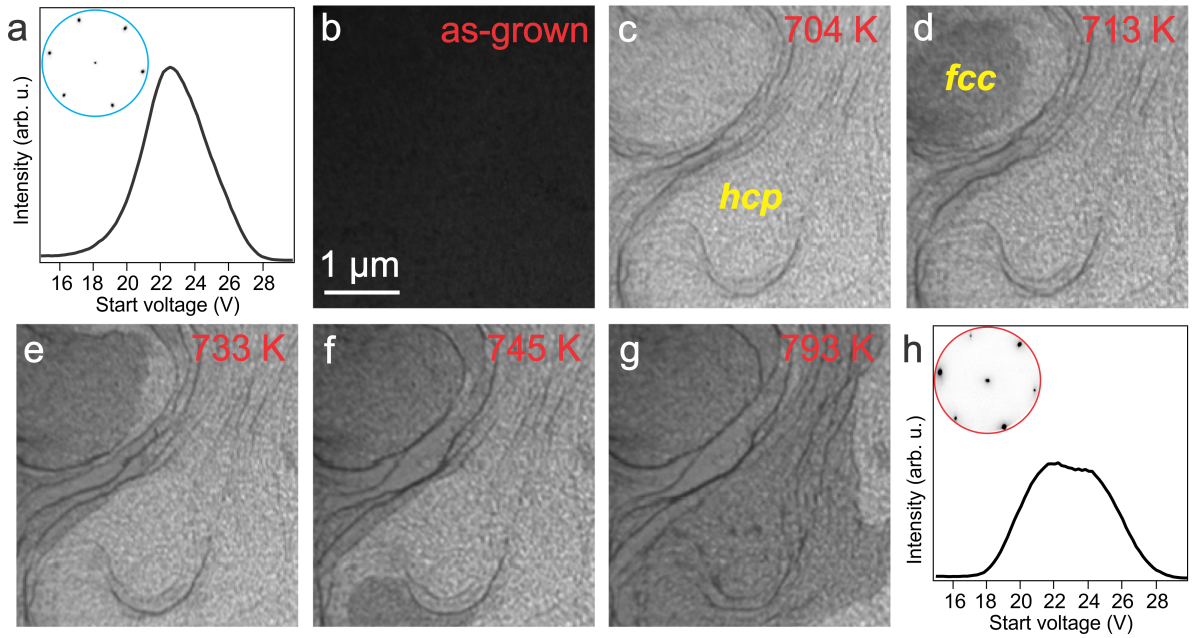

Figure 1: a) LEEM-IV curve of the 50 ML Co on W(110) acquired at room temperature after annealing the as-grown film to 600 K. The inset shows the corresponding µ-LEED pattern (V_{st} = 40 V). b-g) LEEM images (V_{st} = 22 V) acquired during annealing to above the *hcp-fcc* transition starting with the as-grown film. h) LEEM-IV curve acquired at 793 K after the completion of the *hcp-fcc* transition. The inset shows the corresponding µLEED pattern with threefold symmetry (V_{st} = 40 eV).

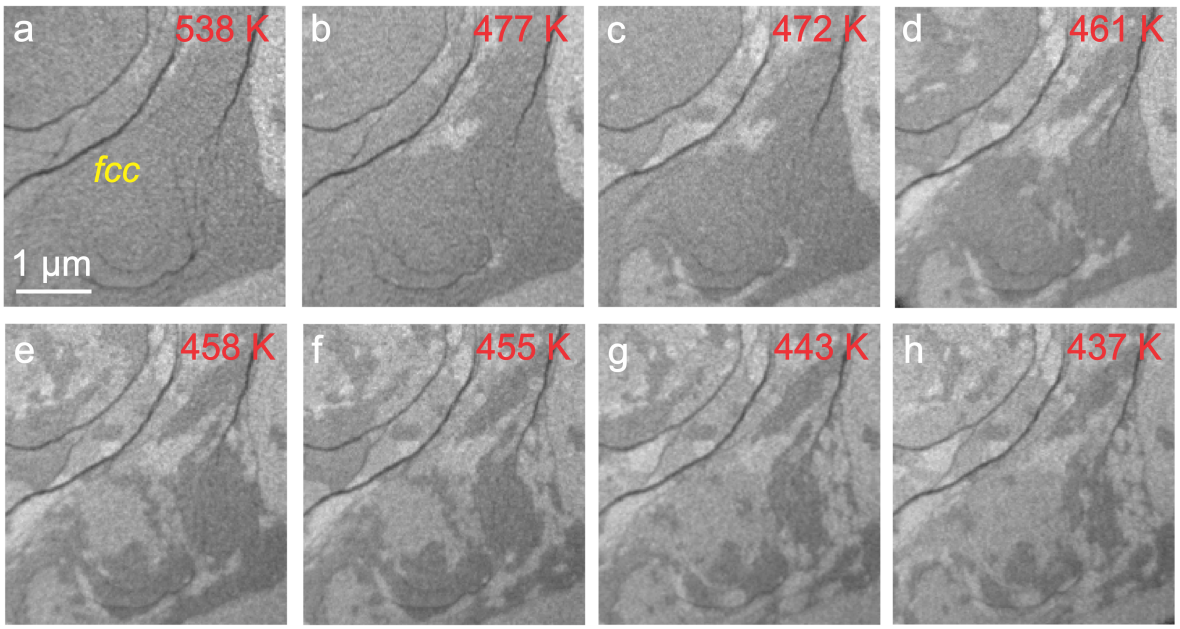

Figure 2: a-h) LEEM images (V_{st} = 22 V) acquired upon cooling the cobalt film on W(110). Cooling rate is about 0.2 K/s.

mean free path of electrons, shorter for Co as compared to Ag,[25] the sensitivity is limited only to a few topmost layers. Thus, there might certainly be more than 3 different stacking configurations, however, the limited sensitivity in LEEM imaging cannot distinguish deeply buried layers below the surface.

The relative abundance of different stacking sequences was determined from the area coverage of regions with characteristic reflectivity curves. According to the data in Figure 3, regions having the same behavior A (45%) and B (48%) cover most of the surface, whereas C (7%) is much less abundant. Structure C is distinguished by a more pronounced shoulder at the low energy side, and a Bragg peak shifted towards higher energies. Based on its more pronounced *fcc*-like shoulder in the low-energy side of the Bragg peak in the LEEM-IV curve and its nearly negligible surface coverage, we tentatively assign it to a stacking sequence in which there is more than one *fcc* layer close to the surface.

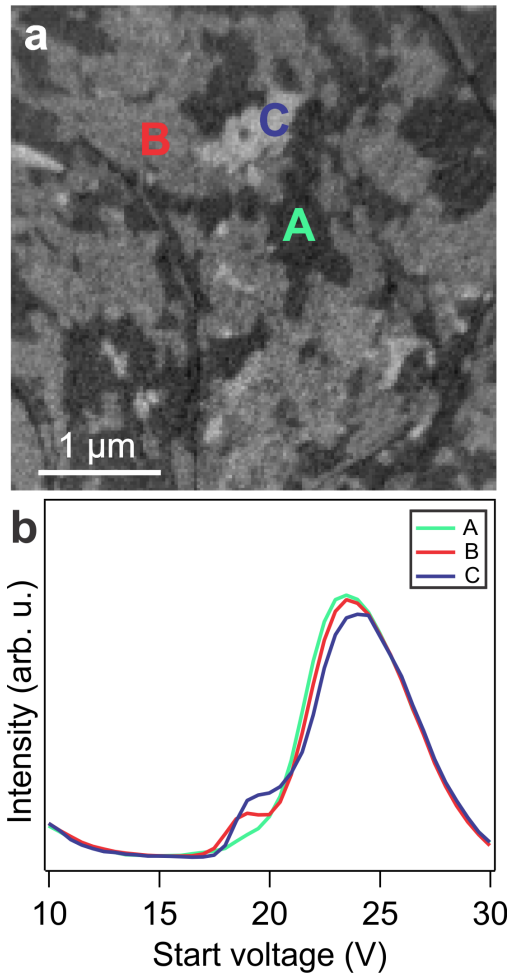

Figure 3: a) LEEM image acquired at V_{st} = 18 V of the sample after cooling down to room temperature. b) LEEM-IV curves of the areas presenting different contrast, as marked by the A, B and C letters.

Interestingly, the *hcp-fcc* transition and even the mere existence of the martensitic transition in the cobalt film depends on the presence of bulk dissolved carbon. To introduce

carbon into the film in a controlled manner, first, a graphene layer was synthesized on top of cobalt *via* chemical vapor deposition using ethylene. The graphene layer was then dissolved by annealing the sample at a temperature of 970 K. Since the atomic density of graphene is twice that of a cobalt layer, the dissolution of a single graphene layer into the 50 ML cobalt film results in a carbon concentration of about 4%. Upon cooling down, the room temperature LEED pattern (Figure S1a) exhibits six sharp diffraction spots with a three-fold behavior. The LEEM-IV curve (Figure S1b) displays a well-defined double-peak feature in the Bragg peak region typical of *fcc* stacking.[20] The differences between the LEEM-IV curves of the clean Co film on W(110) in Figure 1h and the carbon-enriched Co film in Figure S1b likely derive from the different temperatures of measurement (793 K vs. 300 K) and the absence/presence of carbon in the cobalt matrix. These structural properties align with the findings reported by Ishida *et al.*,[21] which suggest that the presence of carbon in the cobalt matrix stabilizes the *fcc* phase even at lower temperatures. This is due to the pronounced difference in carbon solubility in *fcc* Co (1.2%) and in *hcp* Co ($8.74\text{x}10^{-4}$%).[21] Therefore, the carbon enrichment of Co performed at high temperatures (when the crystalline phase is *fcc*) helps preserve the *fcc* phase even upon cooling to room temperature.

Note that, at the relatively high temperatures carried out in this work, we cannot rule out interfacial alloying between Co and W, which may have an influence on the phase stability. Indeed, as we will discuss in the following sections, at even higher temperatures, W dissolves into the Co matrix, influencing the *hcp-fcc* phase competition.

Co/C-W(110): *fcc* vs. *hcp* structure

The growth of cobalt on the carbide-covered W(110) surface proceeds in an entirely different manner in comparison to growth on clean W(110). The carbon-rich tungsten surface was obtained by heating the W(110) crystal to above 2000 K, followed by slow cooling in order to facilitate the surface segregation of bulk carbon. The resulting surface displays an R(15x3) carbon reconstruction as reported in the literature.[26] This reconstruction is characterized by a rather complicated LEED pattern (Figure 4a) consisting of two rotational domains with rectangular symmetry enclosing an angle of 70.5°. As demonstrated previously, on top of this surface Co adopts an *fcc*(100) crystalline arrangement,[27] where the Co[011] direction coincides with the directions predetermined by the carbide structure and the Co[01$\bar{1}$] is dilated by 2.8% as compared to its bulk spacing.

Upon deposition of a cobalt monolayer on top of the C-R(15x3)/W(110) surface, the LEED spots relative to the carbide reconstruction disappear, and no spots other than those of the (1x1) W(110) are visible (Figure 4b). After annealing to 600 K, a faint (1x2) reconstruction appears (Figure 4c). The disappearance of the tungsten carbide spots and the formation of a (1x2) reconstruction upon annealing suggest that the interfacial carbon migrates from the tungsten support to the cobalt layer. Upon deposition of an additional 6 ML Co, aside from the specular beam, only faint and diffuse diffraction features can be seen (Figure 4d). Annealing this surface to 600 K leads to the appearance of sharp LEED spots, identified as two Co *fcc*(100) mirror domains.[28] Moreover, a very clear c(2x2) pattern can be seen and attributed to the formation of surface cobalt carbide in a Co_2C structure (Figure 4e).[28,29] This carbon derives from the W-Co interface and segregates to the surface during annealing. Deposition of additional cobalt, up to a total of 50 atomic layers, leads to similar

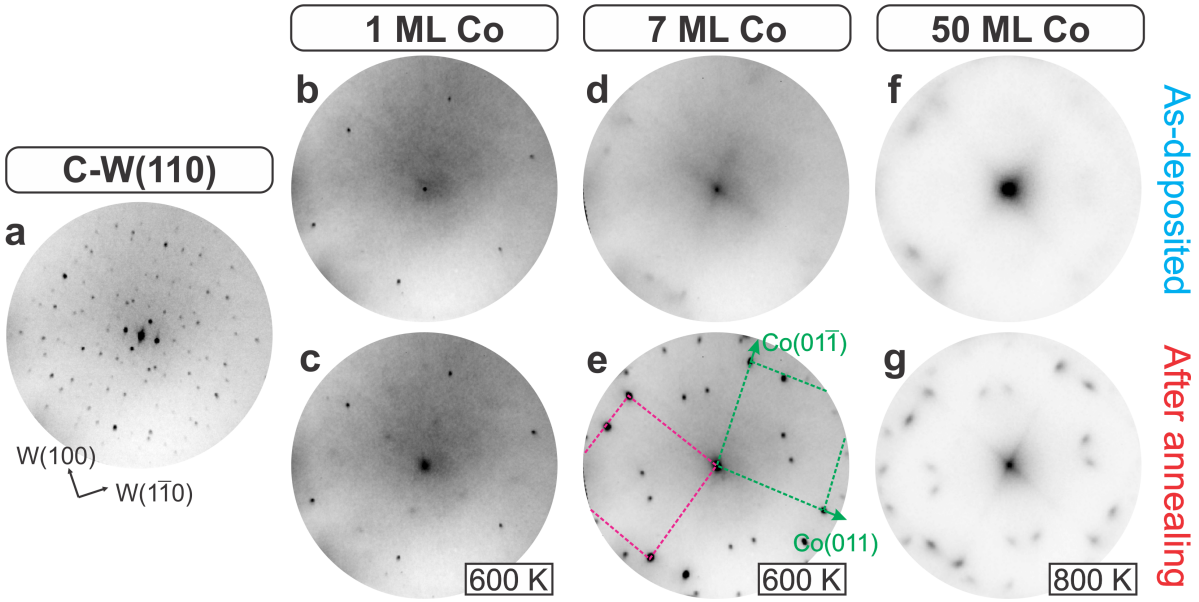

Figure 4: LEED patterns (V_{st} = 40 V) acquired at different deposition/preparation stages of a 50 ML Co film on top of C-R(15x3)/W(110) shown in a). b) 1 ML film as-deposited at room temperature and c) after annealing to 600 K. d) 7 ML film obtained by depositing 6 ML at room temperature on top of the surface in (c), and e) after annealing to 600 K. f) 50 ML film obtained by depositing additional Co at room temperature on top of the surface in (e), and g) after annealing to 800 K. All LEED patterns were acquired at room temperature.

LEED patterns before (Figure 4f) and after (Figure 4g) annealing to 800 K as in the case of 7 ML Co. In distinction from the 7 ML case, the crystalline order of the 50 ML film is recovered only partially upon annealing, with elongated *fcc*(100) spots (Figure 4g).

When the annealing temperature of the 50 ML cobalt film is increased beyond 800 K, a further structural transformation takes place. As visible from the LEEM image sequence (Figure 5a-d), at 850 K, the nucleation and growth of islands (with brighter LEEM contrast at the selected electron energy) takes place. The μLEED pattern acquired on these islands reveals that the surface crystalline structure transformed from quadratic to hexagonal (insets in Figure 5d). The difference is also visible in the LEEM-IV curves (Figure 5e). The curve from the hexagonal islands presents a split Bragg peak reminiscent of the *fcc*(111) LEEM-IV curves. We label these islands as *partially transformed*, considering that annealing at higher temperatures will result in further changes, as will be discussed later.

The transition to the hexagonal surface crystalline arrangement is accompanied by a change in the W $4f$ XPS peak, as seen in Figure 5f, as well as a reduction in the surface carbon signal seen in the C *1s* XPS spectra in Figure 5g. Considering the relatively thick Co film in comparison to the short inelastic mean free path of photoelectrons, the W $4f$ signal can be assigned to W atoms dissolved into the Co matrix. The transformed areas feature a slightly higher W $4f$ intensity as well as a chemical shift towards lower binding energies. As for the C *1s* core level, in the case of the *fcc*(100) film, the peak (Figure 5g top) can be deconvoluted into two components, which can be assigned to the c(2x2) Co_2C (centered at 282.7 eV binding energy)[29] and possibly to disordered carbidic carbon (at 283.2 eV). The low binding energy peak disappears on the hexagonal phase, whereas the high binding energy one remains unvaried (Figure 5g bottom). The high-binding energy peak could be possibly associated with bulk dissolved carbon. Considering that carbon solubility is very low in the pure *hcp* phase, we tentatively attribute the partially transformed regions to a structure featuring a mixed crystalline stacking (*hcp* and *fcc*).

The driving force of the *fcc*(100) to hexagonal structure could be sought in the changes in the bulk dissolved species, *i.e.*, carbon and tungsten. As mentioned above, bulk carbon favors the *fcc* structure,[21] whereas the presence of bulk-dissolved tungsten in Co increases the tendency towards the *hcp* arrangement.[30] The subtle chemical changes within the Co matrix shown in Figure 5 may or may not be responsible for the formation of hexagonal islands. Alternatively, one can hypothesize that the surface carbon found in the c(2x2) structure acts as a surfactant, preventing the transformation of the *fcc*(100) structure to the more stable densely-packed hexagonal phase. Thus, it is possible to speculate that the disappearance of the c(2x2) surface carbon, as seen in Figure 5g, allows the cobalt film to assume a more stable configuration with hexagonal surface symmetry.

Magnetic domains of this thermally-transformed heterogeneous surface can be seen in the XMCD-PEEM images in Figure 6b. The *fcc*(100) film has irregular domains with sub-micron lateral extent. On the other hand, the transformed areas show nearly no magnetic signal with a uniform gray contrast in the dichroism image. Considering it highly unlikely that the Co film is not ferromagnetic, we tentatively attribute the absence of contrast to the magnetization vector oriented along the W[001] direction, thus perpendicular to the x-ray beam propagation direction. For Co films grown on a clean W(110) surface, the Co-W interface is known to induce an in-plane easy axis along the W[1$\bar{1}$0] direction.[27] Thus, in order for the magnetization of the transformed islands to orient along the [001] direction, we

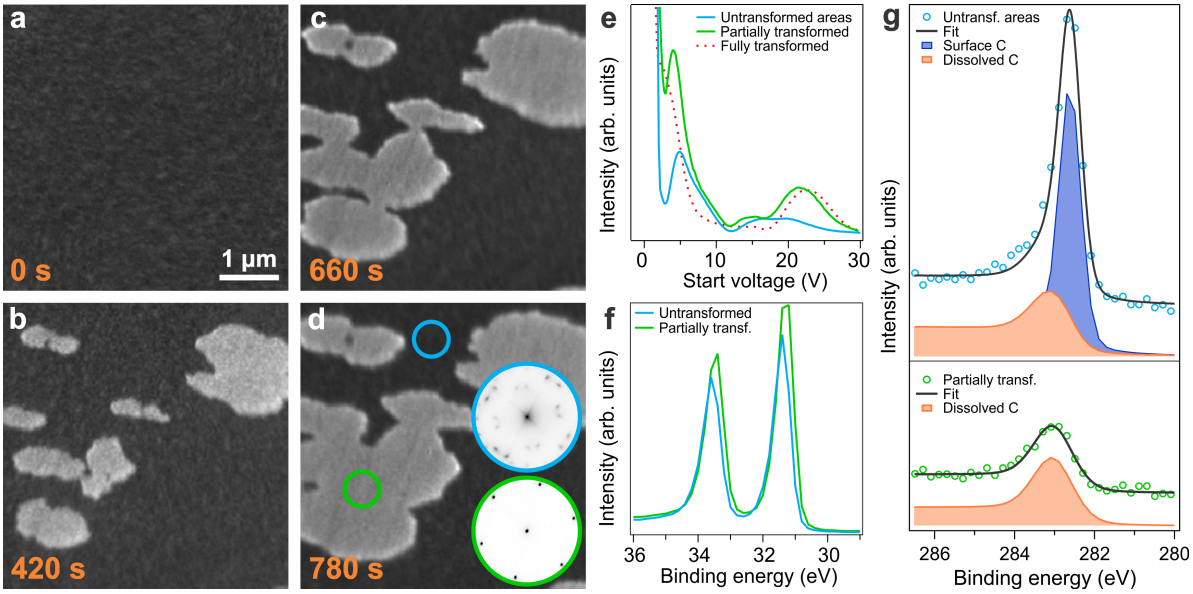

Figure 5: LEEM image sequence (a-d) acquired during the constant temperature (T = 850 K) annealing of a 50 ML Co film deposited on top of tungsten carbide (V_{st} = 2 V). µLEED patterns (V_{st} = 40 V) of the two phases are shown as an inset in panel d). e) LEEM-IV curves of the distinctly transformed and untransformed portions of the surface. Comparison of f) W 4*f* and g) C *1s* XPS spectra (hv = 400 eV) of the untransformed and partially transformed areas.

hypothesize that either the bulk dissolved W and C (as seen in Figure 5) or a subsequent enrichment of the interface with carbon (similar to the situation prior to Co deposition) may be responsible for the magnetic anisotropy along the W[001] direction. The C enrichment of the interface would be in agreement with the disappearance of the surface carbon from the XPS spectra, as shown in Figure 5g (bottom). Nevertheless, a clarification of this point requires further investigation.

The partially-transformed areas further change when the temperature is increased to 900 K. By keeping the sample at this temperature, micron-sized islands displaying distinct contrast form within the areas where Co presents the hexagonal arrangement (Figure 7a). The C *1s* spectrum acquired on these islands is characterized by a sharp and intense peak centered at around 285.0 eV (Figure 7b). Such binding energy is characteristic of Co-supported single-layer graphene.[18] The peak is deconvoluted in two components, centered at 284.9 and 285.2 eV, characteristic of the graphene *"fcc-top"* adsorption configuration.[18] The presence of graphene is also confirmed by looking at the LEEM-IV curve (Figure 7c), which shows the characteristic shape of monolayer graphene on Co. The μ-ARPES spectrum of the graphene islands, acquired at the $\overline{\text{K}}$ point of the surface Brillouin zone, is characterized by a pronounced Dirac cone, with the Dirac point centered at 2.82 eV, in agreement with previous studies.[31,32] Note that, concomitantly, the Co hexagonal regions uncovered by graphene are *fully transformed* to an *hcp*-like phase showing a single Bragg peak in the corresponding LEEM-IV curve. The alignment of graphene on top of the Co film is also confirmed by the µLEED pattern, which is characterized by six sharp and intense first-order peaks (inset of

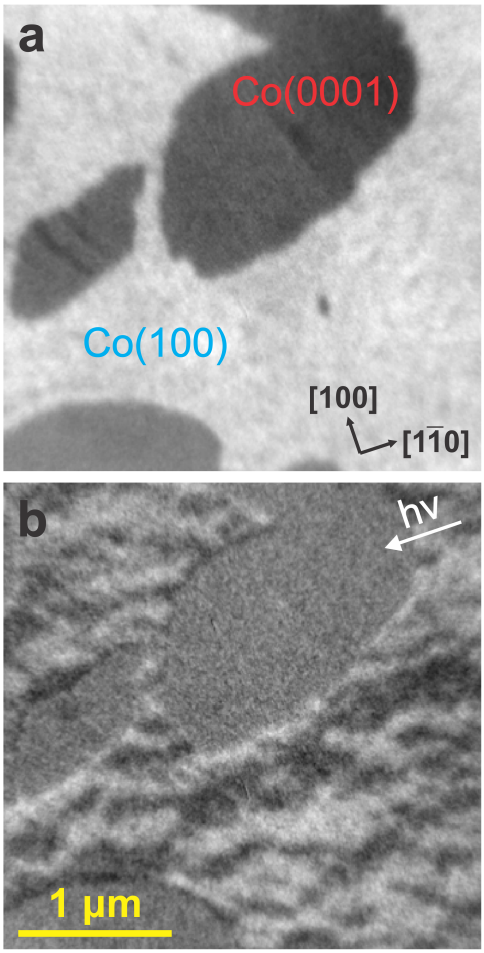

Figure 6: a) Secondary photoelectron PEEM image acquired at 2.5 eV kinetic energy showing similar domains as in Figure 5. b) XMCD-PEEM acquired at the maximum of the Co L_3-edge. The crystalline directions of the W substrate are indicated in the bottom right corner of panel a) and the incidence direction of the X-ray photon beam on top right of panel b).

Figure 7c).

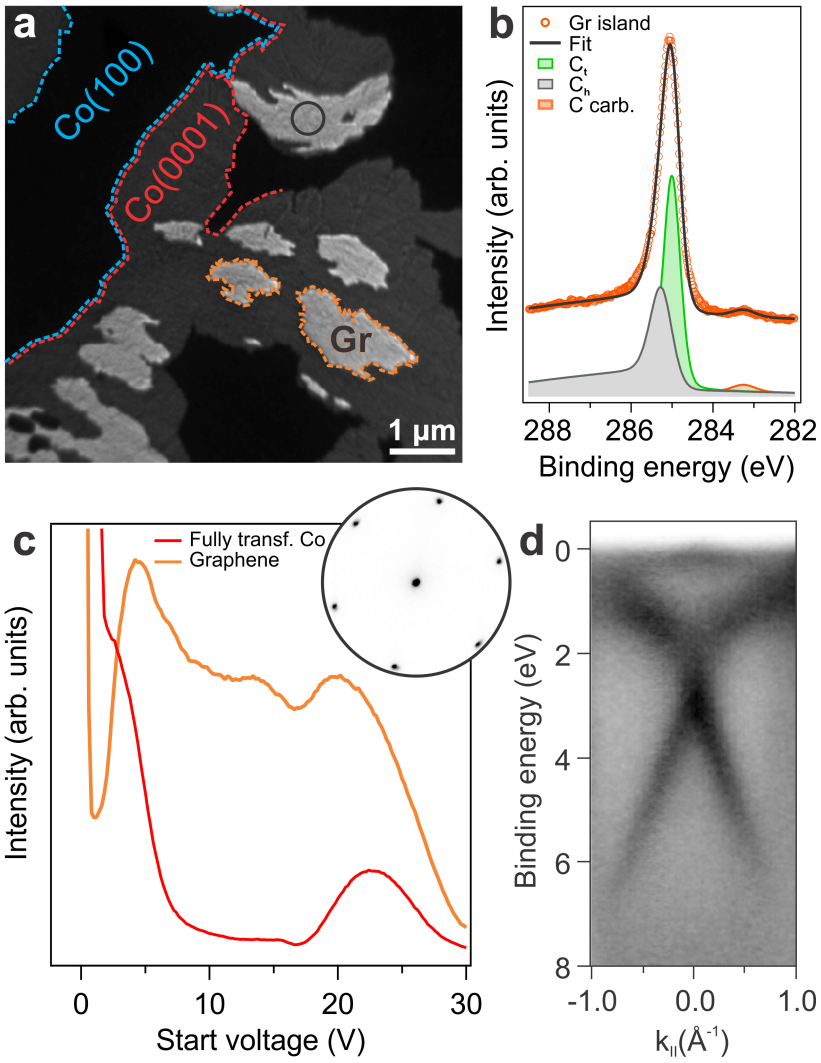

Figure 7: a) LEEM image (V_{st} = 20 V) acquired after annealing the 50 ML cobalt film deposited on top of tungsten carbide to 900 K. b) C *1s* XPS spectrum acquired on the white islands, indicated by the orange dashed lines in a), identified as graphene micron-sized islands. c) LEEM-IV spectra acquired on the graphene islands (and respective LEED pattern as inset) and on the Co substrate (transformed). d) 2D momentum map at the $\overline{\text{K}}$ point of the surface Brillouin zone acquired on a graphene island.

Conclusions

The temperature-induced transformation of a 10 nm thick cobalt film on top of the tungsten support has been presented. For this purpose, two distinct cobalt films were considered, characterized by bulk *hcp* and *fcc* crystalline arrangements as obtained by room temperature deposition of Co on clean and carbon reconstructed W(110), respectively. In the case

of the *hcp* film, the annealing to temperatures above 700 K leads to the occurrence of the well-known *hcp-fcc* phase transition, as revealed by LEEM-IV measurements. By cooling down to room temperature after phase transition completion, partial restoration of the initial *hcp* arrangement and mixed *hcp-fcc* configurations occurs. In the case of *fcc*(100) stacked film, annealing after room temperature deposition allows for an improvement in the crystalline quality. When the temperature is raised above 850 K, an irreversible transition to a hexagonal surface crystalline structure occurs, accompanied by a clear change in the magnetic domain morphology. Further annealing to 900 K leads to graphene formation due to surface segregation of bulk dissolved carbon. Graphene is formed only on the *hcp*(0001) surface portions and is characterized by a perfect epitaxial alignment with the underlying Co substrate.

CVD growth of high quality graphene involves elevated temperatures, thus, understanding thermally-induced changes is crucial for controlling morphology, chemistry and magnetism of the graphene/Co interface in particular. Owing to the recent interest in similar systems, the results presented in this work should help in further developing and optimizing functional heterostructures based on graphene-ferromagnet interfaces.

Experimental section

W(110) single crystal substrate was cleaned by oxygen treatment (1×10^{-6} mbar of molecular oxygen; 1370 K) followed by flashes to above 2250 K in UHV. A 10 nm cobalt film was deposited from a high-purity Co rod in an electron-beam evaporator while keeping the sample at room temperature. The carbon-reconstructed W(110) surface was prepared by flashing the W(110) crystal to above 2000 K, followed by slow cooling, to promote surface segregation of bulk dissolved carbon. The experiments were performed at the Nanospectroscopy beamline of the Elettra Synchrotron in Trieste (Italy). The LEEM and LEED, as well as X-ray Photo-Emission Electron Microscopy (XPEEM) experiments, were carried out using the Spectroscopic Photoemission and Low Energy Electron Microscope (SPELEEM). This instrument combines the structural information from LEEM and LEED with the chemical/magnetic sensitivity of XPEEM.[33,34] The lateral resolution was around 10 nm in LEEM mode and 30 nm in XPEEM.[35,36] The energy resolution in the photoemission experiments was about 0.15 eV.

Supporting Information

The Supporting Information is available free of charge at ...

LEED pattern and LEEM-IV curve of C-enriched cobalt films, additional XPS data at the W 4f core level and LEEM image sequence upon annealing an ultrathin cobalt film.

References

(1) Kaloyeros, A. E.; Pan, Y.; Goff, J.; Arkles, B. Editors' Choice—Review—Cobalt Thin Films: Trends in Processing Technologies and Emerging Applications. *ECS Journal of*

Solid State Science and Technology **2019**, *8*, P119–P152.

(2) Comstock, R. L. Review Modern magnetic materials in data storage. *Journal of Materials Science: Materials in Electronics* **2002**, *13*, 509–523.

(3) Zheng, G. Grain-size effect on plastic flow in nanocrystalline cobalt by atomistic simulation. *Acta Materialia* **2007**, *55*, 149–159.

(4) Bubendorff, J.; Mény, C.; Beaurepaire, E.; Panissod, P.; Bucher, J. Electrodeposited cobalt films: hcp versus fcc nanostructuring and magnetic properties. *The European Physical Journal B* **2000**, *17*, 635–643.

(5) Bouquet, G.; Dubois, B. Influence of the F.C.C. phase retained at room temperature on the mechanical properties of cobalt. *Scripta Metallurgica* **1978**, *12*, 1079–1081.

(6) Blanco-Rey, M. et al. Large Perpendicular Magnetic Anisotropy in Nanometer-Thick Epitaxial Graphene/Co/Heavy Metal Heterostructures for Spin–Orbitronics Devices. *ACS Applied Nano Materials* **2021**, *4*, 4398–4408.

(7) El-Gendy, A. A.; Qian, M.; Huba, Z. J.; Khanna, S. N.; Carpenter, E. E. Enhanced magnetic anisotropy in cobalt-carbide nanoparticles. *Applied Physics Letters* **2014**, *104*.

(8) Harris, V.; Chen, Y.; Yang, A.; Yoon, S.; Chen, Z.; Geiler, A.; Gao, J.; Chinnasamy, C.; Lewis, L.; Vittoria, C.; others High coercivity cobalt carbide nanoparticles processed via polyol reaction: a new permanent magnet material. *Journal of Physics D: Applied Physics* **2010**, *43*, 165003.

(9) Zhang, Y.; Chaubey, G. S.; Rong, C.; Ding, Y.; Poudyal, N.; ching Tsai, P.; Zhang, Q.; Liu, J. P. Controlled synthesis and magnetic properties of hard magnetic CoxC (x=2, 3) nanocrystals. *Journal of Magnetism and Magnetic Materials* **2011**, *323*, 1495–1500.

(10) Valvidares, S. M.; Dorantes-Dávila, J.; Isern, H.; Ferrer, S.; Pastor, G. M. Interface-driven manipulation of the magnetic anisotropy of ultrathin Co films on Pt(111): Substrate deposition of hydrogen and model calculations. *Physical Review B* **2010**, *81*.

(11) Drnec, J.; Vlaic, S.; Carlomagno, I.; Gonzalez, C. J.; Isern, H.; Carlà, F.; Fiala, R.; Rougemaille, N.; Coraux, J.; Felici, R. Surface alloying upon Co intercalation between graphene and Ir(111). *Carbon* **2015**, *94*, 554–559.

(12) Yokoyama, T.; Matsumura, D.; Amemiya, K.; Kitagawa, S.; Suzuki, N.; Ohta, T. Spin reorientation transitions of ultrathin Co/Pd(111) films induced by chemisorption: x-ray magnetic circular dichroism study. *Journal of Physics: Condensed Matter* **2003**, *15*, S537–S546.

(13) Brondin, C. A.; Ghosh, S.; Debnath, S.; Genuzio, F.; Genoni, P.; Jugovac, M.; Bonetti, S.; Binggeli, N.; Stojić, N.; Locatelli, A.; Menteş, T. O. Tailoring Magnetic Anisotropy in Ultrathin Cobalt by Surface Carbon Chemistry. *Advanced Electronic Materials* **2024**, *10*.

(14) Bairagi, K.; Bellec, A.; Repain, V.; Chacon, C.; Girard, Y.; Garreau, Y.; Lagoute, J.; Rousset, S.; Breitwieser, R.; Hu, Y.-C.; Chao, Y. C.; Pai, W. W.; Li, D.; Smogunov, A.; Barreteau, C. Tuning the Magnetic Anisotropy at a Molecule-Metal Interface. *Physical Review Letters* **2015**, *114*.

(15) Song, K.; Li, Z.; Fang, M.; Xiao, Z.; Zhu, Y.; Lei, Q. Recrystallization behavior and phase transformation in a hot-rolled pure cobalt during annealing at the elevated temperature. *Materials Science and Engineering: A* **2022**, *845*, 143178.

(16) Jugovac, M. Morphology and electronic structure of graphene supported by metallic thin films. Dr., Universität Duisburg, Jülich, 2020; Universität Duisburg, Diss., 2020.

(17) Jugovac, M.; Tresca, C.; Cojocariu, I.; Santo, G. D.; Zhao, W.; Petaccia, L.; Moras, P.; Profeta, G.; Bisti, F. Clarifying the apparent flattening of the graphene band near the van Hove singularity. *Physical Review B* **2022**, *105*, L241107.

(18) Jugovac, M.; Genuzio, F.; Gonzalez, E. L.; Stojić, N.; Zamborlini, G.; Feyer, V.; Menteş, T. O.; Locatelli, A.; Schneider, C. M. Role of carbon dissolution and recondensation in graphene epitaxial alignment on cobalt. *Carbon* **2019**, *152*, 4.

(19) Jugovac, M.; Cojocariu, I.; Genuzio, F.; Bigi, C.; Mondal, D.; Vobornik, I.; Fujii, J.; Moras, P.; Feyer, V.; Locatelli, A.; Menteş, T. O. Effect of Residual Carbon on Spin-Polarized Coupling at a Graphene/Ferromagnet Interface. *Advanced Electronic Materials* **2023**, *9*, 2300031.

(20) Jugovac, M.; Menteş, T. O.; Genuzio, F.; Lachnitt, J.; Feyer, V.; Flege, J. I.; Locatelli, A. Sensitivity to crystal stacking in low-energy electron microscopy. *Applied Surface Science* **2021**, *566*, 150656.

(21) Ishida, K.; Nishizawa, T. The C-Co(Carbon-Cobalt) system. *Journal of Phase Equilibria* **1991**, *12*, 417–424.

(22) Bidaux, J.-E.; Schaller, R.; Benoit, W. Study of the h.c.p.-f.c.c. phase transition in cobalt by acoustic measurements. *Acta Metallurgica* **1989**, *37*, 803–811.

(23) Matsumoto, H. Variation in transformation hysteresis in pure cobalt with transformation cycles. *Journal of Alloys and Compounds* **1995**, *223*, L1–L3.

(24) Strauss, B.; Frey, F.; Petry, W.; Trampenau, J.; Nicolaus, K.; Shapiro, S. M.; Bossy, J. Martensitic phase transformation and lattice dynamics of fcc cobalt. *Physical Review B* **1996**, *54*, 6035–6038.

(25) Tanuma, S.; Powell, C. J.; Penn, D. R. Calculations of electron inelastic mean free paths. IX. Data for 41 elemental solids over the 50 eV to 30 keV range. *Surface and Interface Analysis* **2011**, *43*, 689–713.

(26) Varykhalov, A.; Rader, O.; Gudat, W. Structure and quantum-size effects in a surface carbide: W(110)C-R(15x3). *Physical Review B* **2005**, *72*, 115440.

(27) Pinkvos, H.; Poppa, H.; Bauer, E.; Hurst, J. Spin-polarized low-energy electron microscopy study of the magnetic microstructure of ultra-thin epitaxial cobalt films on W(110). *Ultramicroscopy* **1992**, *47*, 339–345.

(28) Bettac, A.; Bansmann, J.; Senz, V.; Meiwes-Broer, K. Structure and magnetism of hcp(0001) and fcc(001) thin cobalt films on a clean and carbon-reconstructed W(110) surface. *Surface Science* **2000**, *454-456*, 936–941.

(29) Gubo, R.; Ren, P.; Yu, X.; Zhang, T.; Wen, X.; Yang, Y.; Li, Y.-W.; (Hans) Niemantsverdriet, J.; (Kees-Jan) Weststrate, C. Similarities and trends in adsorbate induced reconstruction – Structure and stability of FCC iron and cobalt surface carbides. *Applied Surface Science* **2023**, *626*, 157245.

(30) Yin, S. Q.; Wu, Y.; Xu, X. G.; Wang, H.; Wang, J.; Jiang, Y. The effects of tungsten concentration on crystalline structure and perpendicular magnetic anisotropy of Co-W films. *AIP Advances* **2014**, *4*, 127156.

(31) Jugovac, M.; Genuzio, F.; Menteş, T. O.; Locatelli, A.; Zamborlini, G.; Feyer, V.; Schneider, C. M. Tunable coupling by means of oxygen intercalation and removal at the strongly interacting graphene/cobalt interface. *Carbon* **2020**, *163*, 341–347.

(32) Muñiz Cano, B. et al. Rashba-like Spin Textures in Graphene Promoted by Ferromagnet-Mediated Electronic Hybridization with a Heavy Metal. *ACS Nano* **2024**, *18*, 15716–15728.

(33) Locatelli, A.; Bauer, E. Recent Advances in Chemical and Magnetic Imaging of Surfaces and Interfaces by XPEEM. *Journal of Physics: Condensed Matter* **2008**, *20*, 093002.

(34) Bauer, E. *Surface Microscopy with Low-Energy Electrons*; Springer-Verlag New York, 2014.

(35) Locatelli, A.; Aballe, L.; Mentes, T. O.; Kiskinova, M.; Bauer, E. Photoemission Electron Microscopy with Chemical Sensitivity: SPELEEM Methods and Applications. *Surface and Interface Analysis* **2006**, *38*, 1554–1557.

(36) Menteş, T. O.; Zamborlini, G.; Sala, A.; Locatelli, A. Cathode Lens Spectromicroscopy: Methodology and Applications. *Beilstein Journal of Nanotechnology* **2014**, *5*, 1873–1886.

Table of Contents

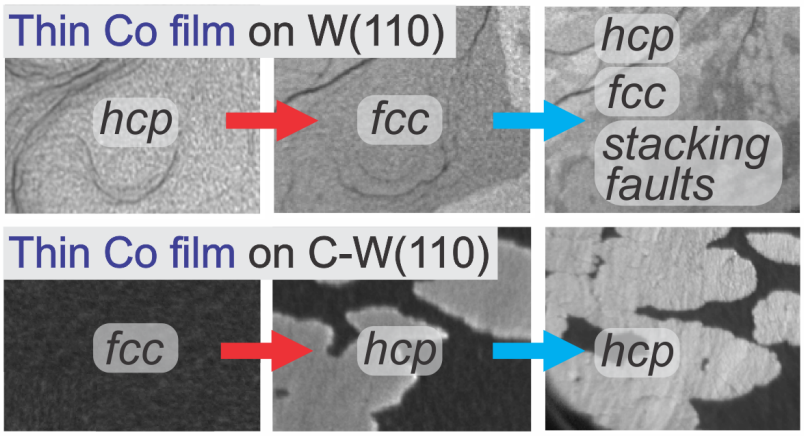

For Table of Contents Use Only.